

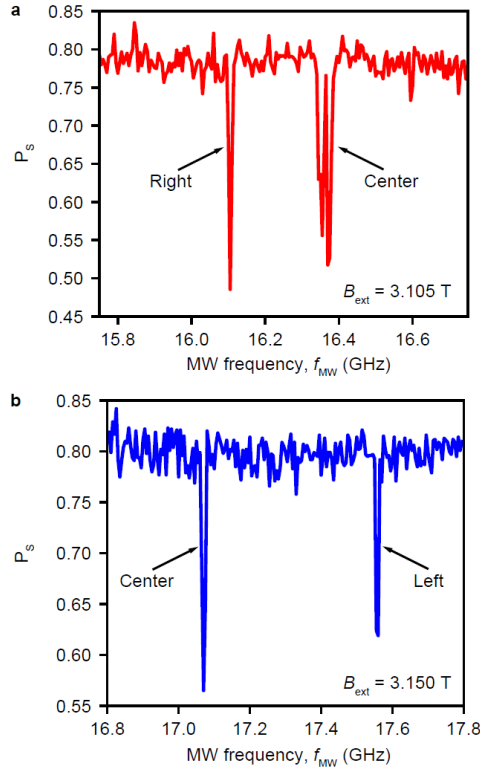
A fast quantum interface between different spin qubit encodings

Noiri *et al.*

Supplementary Note 1: The Zeeman energy difference between the neighboring dots.

To confirm that the oscillation observed in Fig. 1f is driven by ΔE_Z^{ST} , we measure the EDSR spectrum of the center and right dots. We prepare the doubly-occupied singlet state in the right dot and transfer one of the electrons to the center dot adiabatically with respect to ΔE_Z^{ST} to initialize the two spins to $|\uparrow\downarrow\rangle^1$. Then we measure an EDSR spectrum by frequency chirping with a depth of 10 MHz and MW burst length of 20 μs^2 . Here the spectrum is taken at the same gate voltage configuration as the one used for taking data in Fig. 1f. Then the two-spin state is measured by Pauli spin blockade¹. When one of the spins rotates and the two-spin state becomes either one of the polarized triplets, the two electrons remain blocked from returning to the doubly-occupied singlet. Supplementary Fig. 1a shows the MW frequency f_{MW} dependence of the singlet-return probability P_S with $B_{\text{ext}} = 3.105$ T. The two dips around $f_{\text{MW}} \sim 16.1$ GHz and 16.4 GHz correspond to the resonances of the right and center dots, respectively, which are separated by ~ 300 MHz in agreement with the ST precession frequency f^{ST} in Fig. 1f. Because of the strong gate-voltage dependence of ΔE_Z^{ST} (see Methods Sec. 1) the obtained f^{ST} in this measurement is much smaller than that measured in the two-qubit gate experiment ($\Delta E_Z^{\text{ST}}/h = (f_{|\uparrow\rangle}^{\text{ST}} + f_{|\downarrow\rangle}^{\text{ST}})/2 \sim 480$ MHz, see Figs. 2e and 2f).

We also measure the EDSR spectrum of the left and center dots with $B_{\text{ext}} = 3.15$ T as shown in Supplementary Fig. 1b. The two dips of P_S around $f_{\text{MW}} \sim 17.1$ GHz and 17.6 GHz correspond to the resonances of the center and left dots, respectively. As a consequence, we obtain $\Delta E_Z^{\text{QQ}}/h \sim 500$ MHz.



Supplementary Figure 1 | EDSR spectrum measured between the neighboring dots.

a, EDSR spectrum for the center and right dots taken at the same configuration as the one to obtain the data shown in Fig. 1f. The resonance frequency of the center dot is higher than that of the right dot as the local Zeeman field of the center dot induced by the micro-magnet is larger than that of the right dot (Supplementary Fig. 5b). The separation of the resonance condition (~ 300 MHz) is consistent with the ST precession frequency f^{ST} in Fig. 1f. **b**, EDSR spectrum for the left and center dots. The resonance frequencies are separated by ~ 500 MHz.

Supplementary Note 2: Full control of Q_{ST}

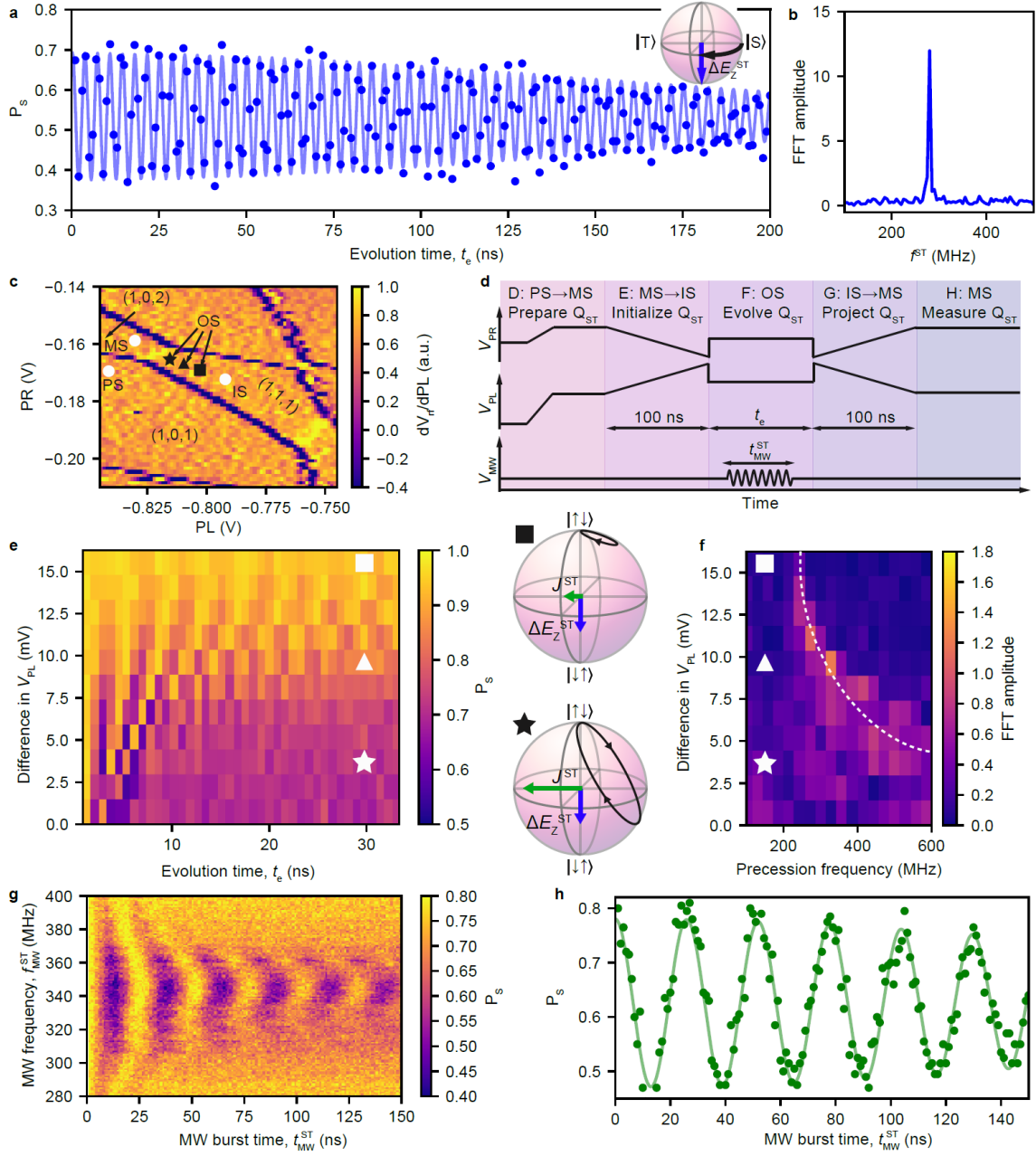
A set of universal quantum gates in a two-qubit system can be constructed by a CPHASE gate and arbitrary single-qubit gates for each qubit. Arbitrary single-qubit gate operations for Q_{LD} can be realized by EDSR (see Fig. 1d). In this section we demonstrate full control of Q_{ST} for completeness. In the following experiment, we quench J^{QQ} to decouple Q_{ST} from Q_{LD} .

The rotation of Q_{ST} around z -axis and x -axis is mediated by ΔE_Z^{ST} and J^{ST} , respectively, as shown in Fig. 1c. Supplementary Fig. 2a shows the precession around z -axis which is measured by initializing Q_{ST} to $|S\rangle$ and projecting the final state along x -axis ($|S\rangle$ or $|T\rangle$) using a pulse sequence shown in Fig. 1g. During the evolution in stage F, J^{ST} is quenched ($\Delta E_Z^{\text{ST}} \gg J^{\text{ST}}$) as the evolution point is far detuned from the resonance of (1,1,1) and (1,0,2) charge states. The fit with the Gaussian decaying

oscillation curve gives $f^{\text{ST}} = 280$ MHz, which is consistent with the FFT spectrum in Supplementary Fig. 2b. Here, the precession visibility is mainly influenced by the error during the state preparation and measurement. The dominant error source is likely the incomplete nonadiabaticity during the state transfers in pulse stages E (for state preparation) and G (for measurement) [the error in charge state discrimination is negligible as described in the main text]. To keep the adiabaticity with respect to the inter-dot tunnel coupling, we choose the pulse rise/fall time of 5 ns, which is too slow to switch J^{ST} nonadiabatically against $\Delta E_Z^{\text{ST}}/h \sim 280$ MHz. As a result, the prepared state in stage E is inclined to $|\uparrow\downarrow\rangle$ from $|S\rangle$, decreasing the ST precession visibility even though the system is coherent. This error could be suppressed by, instead, initializing to $|\uparrow\downarrow\rangle$ and subsequently rotating around y -axis^{3,4}, although we do not experimentally pursue this alternative preparation. We also note that the ST precession visibility can decrease due to the state leakage to non-qubit states during turning on and off J^{QQ} . We avoid this problem by adiabatically turning on and off J^{QQ} with respect to ΔE_Z^{QQ} (see Supplementary Note 3) and obtain a similar visibility of the ST precessions measured in J^{QQ} on (Figs. 2e and 2f) and off (Fig. 1f).

Next we demonstrate the qubit control around x -axis using a pulse sequence shown in Supplementary Fig. 2d. Here Q_{ST} is initialized to $|\uparrow\downarrow\rangle$ by slow adiabatic passage, kept at a detuned point (stage F) and projected along z -axis ($|\uparrow\downarrow\rangle$ or $|\downarrow\uparrow\rangle$) using the reverse process of the initialization^{1,5}. Supplementary Fig. 2e shows the evolution of Q_{ST} as a function of the detuned point. As the point approaches the resonance of (1,1,1) and (1,0,2), J^{ST} increases and the rotation axis is inclined toward the x direction, eventually realizing the rotation around the x -axis for $\Delta E_Z^{\text{ST}} \ll J^{\text{ST}}$. In this scheme, however, the dephasing time decreases as J^{ST} is increased due to the enhanced exchange noise⁶. To improve the control quality, we employ resonantly driven rotation of Q_{ST} around the x -axis in the rotating frame^{3,4}. Here we choose a detuned point where $\Delta E_Z^{\text{ST}} > J^{\text{ST}}$ is satisfied and modulate

J^{ST} at the qubit resonance frequency, $\sqrt{J^{\text{ST}^2 + \Delta E_Z^{\text{ST}^2}}/h$, by applying a MW burst to PC gate (see Fig. 1a). Then Q_{ST} exhibits the Rabi rotation at a frequency proportional to the modulation amplitude. Supplementary Fig. 2g shows the MW frequency dependence of the Rabi oscillations. We find the resonance at $f_{\text{MW}}^{\text{ST}} = 345$ MHz, where we see a clear coherent oscillation as shown in Supplementary Fig. 2h. These results demonstrate full control of Q_{ST} and therefore, our system is capable of universal two-qubit manipulations.



Supplementary Figure 2 | Full control of Q_{ST} .

a, Precession around the z -axis due to ΔE_Z^{ST} by quenching J^{ST} . The data and the fitting curve is the same as the one shown in Fig. 1f. The fitting gives the dephasing time of 207 ± 11 ns. **b**, FFT spectrum of **a** showing a peak at $f^{ST} = 280$ MHz in agreement with the fitting (see Fig. 1f). **c**, Stability diagram of the TQD used for demonstrating the full control of Q_{ST} . [The gate voltage configuration differs from Fig. 1b and the data were taken in a different cool-downs]. **d**, Pulse sequence used to demonstrate the control of Q_{ST} around x -axis by J^{ST} . In stages E and G, $|\uparrow\downarrow\rangle$ and $|\downarrow\uparrow\rangle$ and $|\uparrow\uparrow\rangle$ are interconverted adiabatically, allowing a z -axis readout of Q_{ST} by the Pauli spin blockade⁵. For taking the data in **g**, a MW burst with frequency f_{MW}^{ST} and duration t_{MW}^{ST} is applied to the PC

gate at stage F. **e**, The state evolution during the Q_{ST} rotation. The trajectories of Q_{ST} at detuned points marked by the square and star symbols are illustrated in the laboratory-frame Bloch spheres shown on the right. **f**, FFT spectra of the data in **e**. The white dashed curve is an eye guide of the spectral peaks drawn at $\sqrt{J^{ST^2} + \Delta E_Z^{ST^2}}/h$. **g**, A MW frequency dependence of resonantly driven rotation, taken at the point shown by the black triangle in **c**. **h**, Rabi oscillation of Q_{ST} measured at the resonance, $f_{MW}^{ST} = 345$ MHz.

Supplementary Note 3: The origin of the two-qubit gate.

In this section we discuss the conditions for Eq. 1 to be a good approximation⁷. The general Hamiltonian of the three-spin system in the (1,1,1) charge state under a magnetic field is given by

$$\mathcal{H} = \mathcal{H}_Z + \mathcal{H}_J \quad (1)$$

$$\mathcal{H}_Z = -E_Z \hat{\sigma}_z^{LD}/2 - (\Delta E_Z^{QQ} + E_Z) \hat{\sigma}_z^C/2 - (\Delta E_Z^{ST} + \Delta E_Z^{QQ} + E_Z) \hat{\sigma}_z^R/2 \quad (2)$$

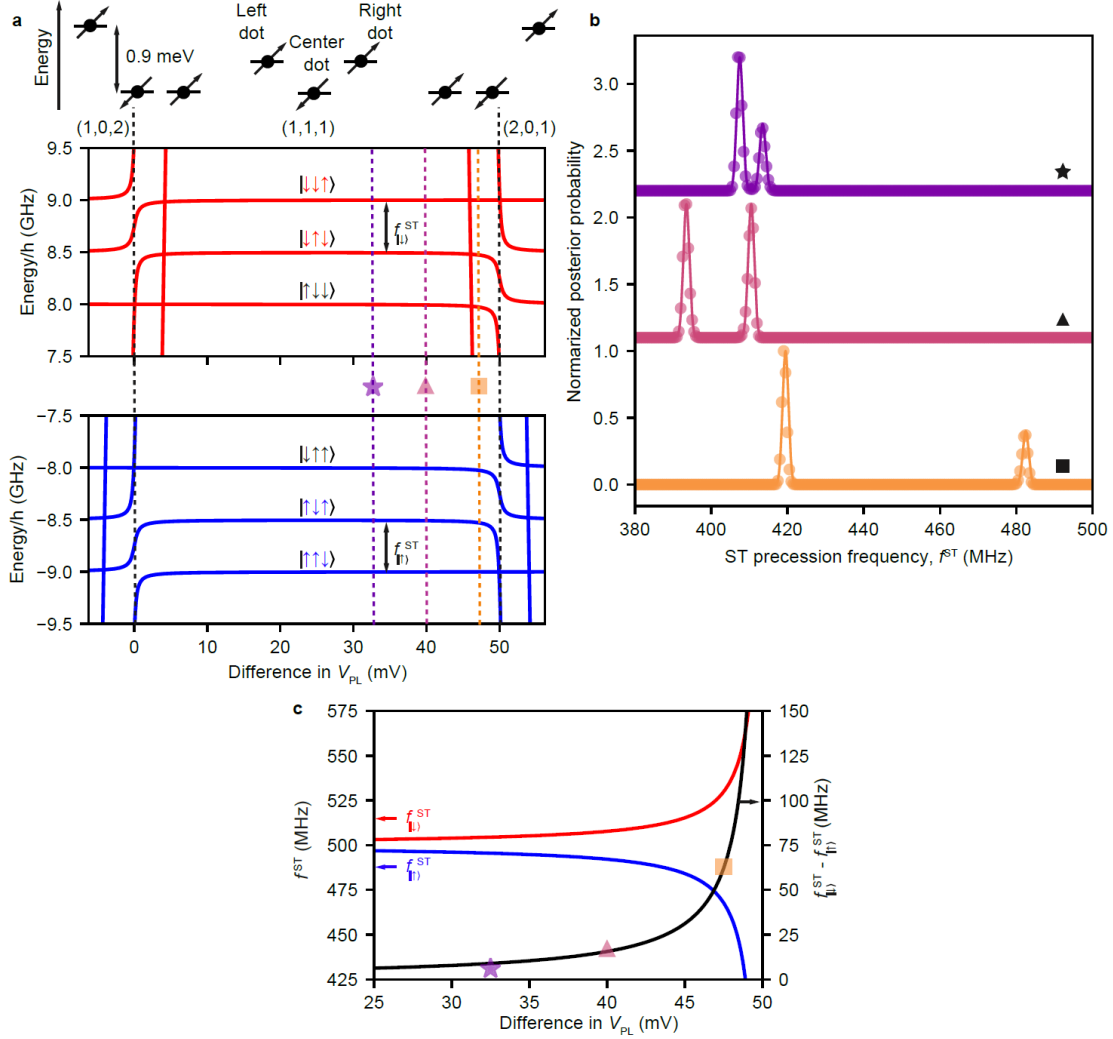
$$\mathcal{H}_J = J^{QQ}(\hat{\boldsymbol{\sigma}}^{LD} \cdot \hat{\boldsymbol{\sigma}}^C - \mathbf{1})/4 + J^{ST}(\hat{\boldsymbol{\sigma}}^C \cdot \hat{\boldsymbol{\sigma}}^R - \mathbf{1})/4 \quad (3)$$

where \mathcal{H}_Z and \mathcal{H}_J represent the Zeeman energy term and the exchange coupling, respectively. Here $\hat{\boldsymbol{\sigma}}^{LD}$ ($\hat{\sigma}_z^{LD}$), $\hat{\boldsymbol{\sigma}}^C$ ($\hat{\sigma}_z^C$) and $\hat{\boldsymbol{\sigma}}^R$ ($\hat{\sigma}_z^R$) are the Pauli operators (and their z -component) of the spin in the left, center and right dots, respectively. E_Z is the Zeeman energy of the spin in the left dot. ΔE_Z^{QQ} and ΔE_Z^{ST} are the Zeeman energy difference between the left and center dots and between the right and center dots, respectively. We assume exchange couplings only between neighboring dots, J^{QQ} (J^{ST}) between the left (right) and center dots. The Zeeman energy difference between the neighboring dots ΔE_Z^{QQ} (ΔE_Z^{ST}) competes with the exchange coupling J^{QQ} (J^{ST}). In the case of $\Delta E_Z^{QQ}, \Delta E_Z^{ST} \gg J^{QQ}, J^{ST}$ which is the case in our experiments, the three-spin eigenstates are well approximated by three isolated spins $|\sigma_z^{LD} \sigma_z^C \sigma_z^R\rangle$ rather than the exchange dominated states of the doublets and quadruplets⁸. Those three-spin states, mainly determined by \mathcal{H}_Z , are perturbed by \mathcal{H}_J . At the two-qubit interaction point which is near the resonance of (1,1,1) and (2,0,1) charge state, $J^{QQ} \gg J^{ST} \sim 0$ is satisfied and therefore the second term of Supplementary Eq. 3 is neglected. Furthermore, we apply large external magnetic field such that $E_Z \gg \Delta E_Z^{QQ}, \Delta E_Z^{ST}$ to energetically separate $|\uparrow\uparrow\uparrow\rangle$ and $|\downarrow\downarrow\downarrow\rangle$ from the two-qubit subspace of $|\uparrow\uparrow\downarrow\rangle, |\uparrow\downarrow\uparrow\rangle, |\downarrow\uparrow\downarrow\rangle$ and $|\downarrow\downarrow\uparrow\rangle$, with the consequence that the leakage from the qubit states to those fully spin-polarized states becomes negligible. The state leakage to the other non-qubit states, $|\downarrow\uparrow\uparrow\rangle$ and $|\uparrow\downarrow\downarrow\rangle$, is also suppressed by adiabatically turning on and off J^{QQ} with respect to ΔE_Z^{QQ} ⁹. Therefore we can restrict ourselves only to the two-qubit subspace under the condition of $E_Z \gg \Delta E_Z^{QQ}, \Delta E_Z^{ST} \gg J^{QQ} \gg J^{ST}$. Here the first, second and third terms of Supplementary Eq. 2 are simplified to the first and the second terms of Eq. 1. In addition, the first term of Supplementary Eq. 3 can be approximated by the last term of Eq. 1. In our experiment, the relevant parameter values at the two-qubit interaction configuration are $E_Z/h \sim 17$ GHz, $\Delta E_Z^{QQ}/h \sim$

$\Delta E_Z^{ST}/h \sim 0.5$ GHz, $J^{QQ}/h \sim 0.09$ GHz and $J^{ST}/h \sim 0$ GHz and therefore the above conditions are satisfied and Eq. 1 is a good approximation.

Supplementary Note 4: The controllability of J^{QQ} by the gate voltages.

In this section we discuss the three-spin state energy diagram in our experimental setup and its gate voltage dependence. Supplementary Fig. 3a shows the calculated energy levels as a function of the gate voltages V_{PL} and V_{PR} which are changed to detune the energies between the outer dots while keeping the center dot energy level fixed^{1,8}. Here we assume a common inter-dot tunnel coupling t between neighboring dots and Zeeman energies $E_Z/h = 17$ GHz, $\Delta E_Z^{QQ}/h = \Delta E_Z^{ST}/h = 0.5$ GHz. The red and blue curves in Supplementary Fig. 3c show the Q_{LD} state dependent ST precession frequencies $f_{\sigma_{LD}}^{ST}$ as a function of V_{PL} . Supplementary Fig. 3b shows the $f_{\sigma_{LD}}^{ST}$ spectra measured at the three interaction points marked by the star, triangle and square symbols in Fig. 1b. Here we obtain the spectra by Bayesian estimation^{3,10} (see also Methods) instead of the FFT used in Fig. 2c. By fitting the spectra, we obtain splittings of $f_{|\downarrow\rangle}^{ST}$ and $f_{|\uparrow\rangle}^{ST}$, $f_{|\downarrow\rangle}^{ST} - f_{|\uparrow\rangle}^{ST} = 6.08 \pm 0.01, 17.18 \pm 0.01$ and 63.13 ± 0.01 MHz for each point. These values are plotted in Fig. 2d. Then we fit the obtained gate voltage dependence of $f_{|\downarrow\rangle}^{ST} - f_{|\uparrow\rangle}^{ST}$ with the model curve calculated from Supplementary Fig. 3a as shown by the black curve. We find an agreement between the theory model and the data upon choosing $t = 1.2$ GHz and the lever arm of the detuning energy against V_{PL} of 18 meV/V.



Supplementary Figure 3 | Three-spin state energy diagram.

a, Three-spin state energy diagram as a function of V_{PL} with a corresponding energy level of each dot. The voltages are plotted as difference from the degeneracy of (1,1,1) and (1,0,2) charge states, at $(V_{PL}, V_{PR}) = (-348 \text{ mV}, -208 \text{ mV})$ (see Fig. 1b). The degeneracy between (1,1,1) and (2,0,1) charge states is located at $(V_{PL}, V_{PR}) = (-298 \text{ mV}, -248 \text{ mV})$. We assume that the energy difference between (1,0,2) and (2,0,1) charge states, corresponding to the difference in (V_{PL}, V_{PR}) being (50 mV, -40 mV), is 0.9 meV. This gives an agreement with the measured data (three symbols) in Fig. 2d. The positions of the interaction points used in Figs. 2c and 2d are shown by dashed lines with the corresponding symbols. **b**, Posterior probability of f^{ST} calculated by Bayesian estimation from the data used in Fig. 2c (traces offset for clarity). Each trace is normalized by its maximum. The solid curves are the fit with the weighted sum of two Gaussian distributions. **c**, $f_{\sigma_z^L D}^{ST}$ (the red and blue curves) and $f_{\sigma_z^L D}^{ST} - f_{|\uparrow\rangle}^{ST}$ (the black curve) extracted from **a** as a function of V_{PL} . The three symbols are obtained from **b**.

Supplementary Note 5: The model of the ST precession under J^{QQ} .

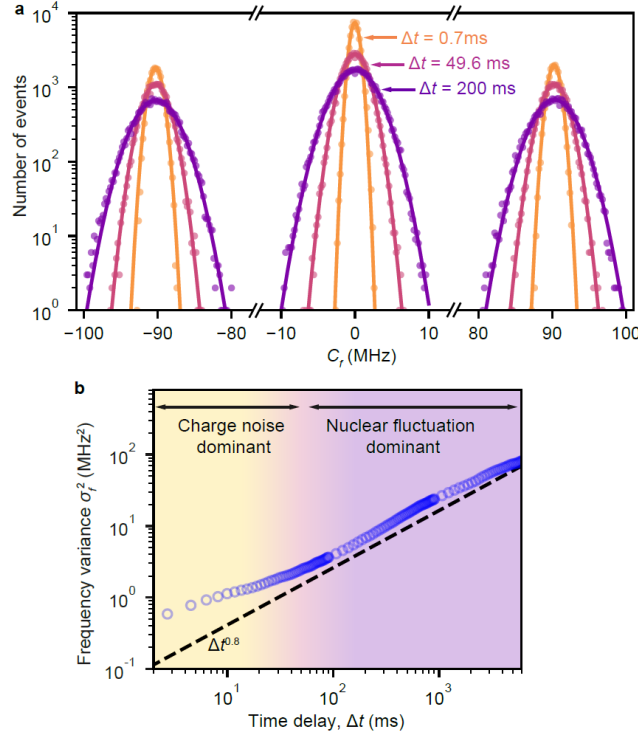
Here we explain the ST precession model $P_{\text{S,model}}$ in Eq. 2. We assume that $P_{\text{S,model}}$ is a Gaussian decaying oscillation function¹¹ with an oscillation frequency $f_{\sigma_z^{\text{LD}}}^{\text{ST}}$. The decay time T_2^* is the dephasing time of Q_{ST} determined by fluctuating ϕ^{ST} (due to nuclear field and charge noise) occurring within a single pulse cycle of 700 μs (in the black dashed square in Fig. 2b). The oscillations amplitude $a = 0.218$ and the mean value of the oscillation $b = 0.511$ are determined by three factors, i.e., initialization error of Q_{ST} , tilt of the precession axis determined by $J^{\text{ST}}/\Delta E_Z^{\text{ST}}$ and the readout error of Q_{ST} . The phase of Q_{ST} is described by two terms, Q_{LD} -controlled phase $\phi_{\sigma_z^{\text{LD}}} = -\pi\sigma_z^{\text{LD}}J^{\text{QQ}}(t_{\text{int}} + t_0)/h$ and the single-qubit phase $\phi^{\text{ST}} = 2\pi\Delta E_Z^{\text{ST}}(t_{\text{int}} + t_{\text{ramp}})/h + \phi_0$ which accumulates independently from Q_{LD} . Here t_0 accounts for the effective total time for turning on and off J^{QQ} with voltage pulses. The estimated value of $t_0 = 1.53$ ns found by MLE is much smaller than the voltage pulse ramp time of $t_{\text{ramp}} = 24$ ns as J^{QQ} rapidly increases only near the resonance of (1,1,1) and (2,0,1) charge states (see Fig. 2d). Since ΔE_Z^{ST} also varies during the voltage ramps due to the inhomogeneity of the MM-induced magnetic field, an additional phase ϕ_0 is necessary to properly describe ϕ^{ST} . We note the fluctuation of ϕ_0 is independent from that of ΔE_Z^{ST} due to the inhomogeneity of the nuclear Overhauser field. In this model, any possible fluctuation of J^{QQ} due to charge noise is equivalent to an additional fluctuation in ΔE_Z^{ST} and ϕ_0 , and therefore does not have to be parametrized separately.

Supplementary Note 6: Coherence of the two qubits.

Here we discuss possible limiting factors of T_2^* in Eq. 2 following the analysis presented in Ref. 10. T_2^* is the dephasing time caused by the two fluctuators: the nuclear field and charge noise, within the data acquisition time. To evaluate the characteristic time scale of the fluctuation, we calculate the time correlator of $f_{\sigma_z^{\text{LD}}}^{\text{ST}}$, $C_f(\Delta t) = f_{\sigma_z^{\text{LD}}}^{\text{ST}}(t + \Delta t) - f_{\sigma_z^{\text{LD}}}^{\text{ST}}(t)$ as a function of time delay, Δt (see Ref. 10). The histogram of the correlator has a main peak at $C_f = 0$ MHz and two side peaks at $\pm J^{\text{QQ}}/h = \pm 90$ MHz due to flip-flops of the Q_{LD} state (Supplementary Fig. 4a). All of the peaks show Gaussian distribution and their variance $\sigma_f^2(\Delta t)$, which has similar values between each peak, determines T_2^* as $T_2^*(\Delta t) \propto 1/\sigma_f(\Delta t)$. Supplementary Fig. 4b shows the Δt dependence of σ_f^2 calculated from the main peak of C_f . We identify two different regimes, 50 ms $< \Delta t$ and $\Delta t < 50$ ms. For 50 ms $< \Delta t$, the variance shows the dependence $\sigma_f^2 \propto \Delta t^{0.8}$ similar to Ref. 10, where the diffusion of nuclear spins is suggested to be the origin. In this regime, the variance and thereby T_2^* are limited by the Overhauser field fluctuation. On the other hand, in $\Delta t < 50$ ms, the variance displays saturation. This suggests another noise source with a larger high-frequency tail, which we believe is due to the charge noise becoming dominant. Therefore we suppose that in our two-qubit gate experiment, the coherence of Q_{ST} is limited by charge noise. In this regime, the observed

dephasing time dominates the dephasing of the whole two-qubit system, and therefore we conclude that the dephasing time of our CPHASE gate is 211 ns.

In contrast, for the ST precession measurement data shown in Figs. 2e and 2f, a much longer data acquisition time of 451 ms results in $T_2^* \approx 70$ ns, limited by the nuclear spins.



Supplementary Figure 4 | Variance of the ST precession frequency.

a, Histogram of the time correlator of the estimated ST precession frequency having a main peak at zero frequency and two side peaks at $\pm J^{\text{QQ}}/h$. Each peak fits well to a Gaussian distribution. **b**, Δt dependence of the estimated ST precession frequency variance calculated from the main peak of C_f (blue open circles). The dotted line is $\sigma_f^2 \propto \Delta t^{0.8}$ reflecting the nuclear spin diffusion¹⁰.

Supplementary Note 7: The unconditional phase accumulation during the CPHASE gate.

Here we describe the condition where the CPHASE gate including the single-qubit phase gates of Q_{ST} and Q_{LD} is realized^{7,12}. From Eqs. 1 and 2, the two-qubit interaction in the basis states of $|\uparrow\uparrow\rangle, |\uparrow\downarrow\rangle, |\downarrow\uparrow\rangle$ and $|\downarrow\downarrow\rangle$ is given by the unitary operation,

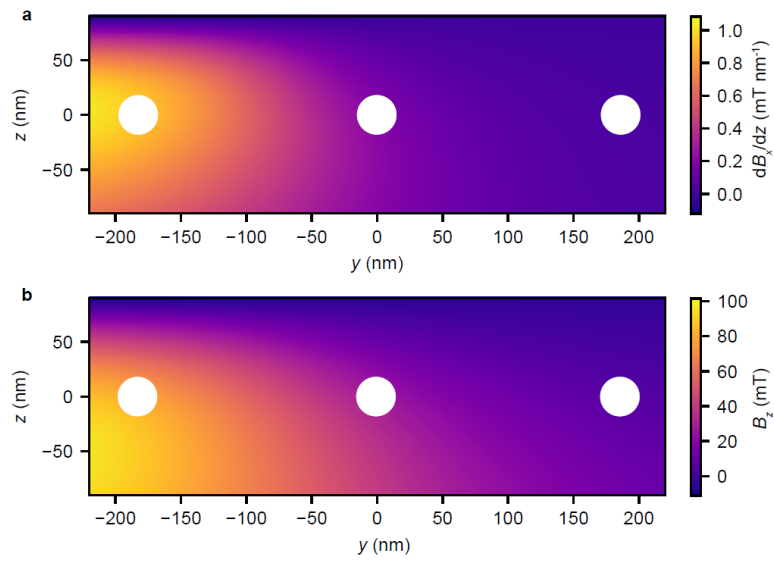
$$\begin{aligned}
U(t_{\text{int}}) &= Z^{\text{LD}}(-\phi^{\text{LD}})Z^{\text{ST}}(-\phi^{\text{ST}}) \begin{pmatrix} 1 & 0 & 0 & 0 \\ 0 & e^{-i\phi_{|\uparrow\rangle}} & 0 & 0 \\ 0 & 0 & e^{i\phi_{|\downarrow\rangle}} & 0 \\ 0 & 0 & 0 & 1 \end{pmatrix} \\
&= Z^{\text{LD}}(-\phi^{\text{LD}} + \phi_{|\downarrow\rangle})Z^{\text{ST}}(-\phi^{\text{ST}} - \phi_{|\uparrow\rangle}) \begin{pmatrix} 1 & 0 & 0 & 0 \\ 0 & 1 & 0 & 0 \\ 0 & 0 & 1 & 0 \\ 0 & 0 & 0 & e^{-i(\phi_{|\downarrow\rangle} - \phi_{|\uparrow\rangle})} \end{pmatrix} \quad (4)
\end{aligned}$$

where $Z^{\text{LD}}(\phi)$ and $Z^{\text{ST}}(\phi)$ represent qubit rotation around the z -axis by angle ϕ for Q_{LD} and Q_{ST} , respectively. Up to single-qubit phases (neglecting $Z^{\text{LD}}(-\phi^{\text{LD}} + \phi_{|\downarrow\rangle})$ and $Z^{\text{ST}}(-\phi^{\text{ST}} - \phi_{|\uparrow\rangle})$), the CPHASE gate is realized for any integer n such that $\phi_{\text{C}} = \phi_{|\downarrow\rangle} - \phi_{|\uparrow\rangle} = 2\pi J^{\text{QQ}}(t_{\text{int}} + t_0)/h = \pi(2n + 1)$. This condition is met in our experiment with $t_{\text{int}} = 4.0 + 11n$ ns where 4.0 ns comes from the initial phase due to a finite value for t_0 .

More strictly, to construct the CPHASE gate without ignoring the single-qubit phases, each single-qubit phase should satisfy $\phi^{\text{LD}} - \phi_{|\downarrow\rangle} = 2\pi l$ and $\phi^{\text{ST}} + \phi_{|\uparrow\rangle} = 2\pi m$ where l and m are integers. This can be realized by a phase gate of Q_{ST} and Q_{LD} or a decoupled CPHASE gate^{13,14}, although we do not perform them in our experiment.

Supplementary Note 8: The quality factor of the CPHASE gate.

Here we discuss the performance of the CPHASE gate. A convenient figure of merit is the quality factor Q representing the number of possible CPHASE gate operations within the dephasing time. It is evaluated to be $Q = 2J^{\text{QQ}}T_2^*/h = 38$ in our experiment. For comparison, Ref. 13 uses a two-qubit gate with $Q \sim 10$ and evaluates the lower bound of the gate fidelity to be 85 % extracted from the Bell state tomography. Our value of Q therefore suggests that our CPHASE gate fidelity could be potentially higher than 85 %. However, the gate fidelity has to be characterized by more elaborate approaches such as process tomography or randomized benchmarking in future experiments. Si-based devices with much better single-qubit gate fidelity will allow these detailed characterizations.



Supplementary Figure 5 | Local magnetic field simulation.

a, Simulated distribution of the slanting field dB_x/dz created by a MM for the design shown in Fig. 1a calculated by the boundary integral method¹⁵. The white circles indicate the positions of the three dots from the device lithography design. **b**, Simulated local Zeeman field B_z .

Q_{LD}	Interaction time index k	$k = 1$...	$k = 100$
	Pulse cycle index m	$(t_{\text{int}} = 0.83 \text{ ns})$		$(t_{\text{int}} = 83 \text{ ns})$
$\sigma_z^{\text{LD}} = \uparrow\rangle$	$m = 1$	$r_{m=1}^{k=1}$...	$r_{m=1}^{k=100}$
	\vdots	\vdots	...	\vdots
	$m = 2000$	$r_{m=2000}^{k=1}$...	$r_{m=2000}^{k=100}$
$\sigma_z^{\text{LD}} = \downarrow\rangle$	$m = 2001$	$r_{m=2001}^{k=1}$...	$r_{m=2001}^{k=100}$
	\vdots	\vdots	...	\vdots
	$m = 4000$	$r_{m=4000}^{k=1}$...	$r_{m=4000}^{k=100}$

Supplementary Table 1 | Data structure for the ST precession parameter estimation.

Collected data set for the ST precession parameter estimation. m , k and r_m^k represent the pulse cycle index, the interaction time index $t_{\text{int}}(k) = 0.83k \text{ ns}$ and the readout result of Q_{ST} : $r_m^k = 1$ (0) for $Q_{\text{ST}} = |S\rangle$ ($|T\rangle$). For each interaction time and Q_{LD} state, we have 2000 readout results whereas for each pulse cycle, we have 100 readout results of Q_{ST} .

Parameter	Minimum	Maximum	Number of discretized points	Pulse-cycle-dependency
a	0.208	0.223	16	No
b	0.501	0.516	16	
J^{QQ}/h (MHz)	89.8	91.3	16	
t_0 (ns)	1.4	1.7	16	
T_2^* (ns)	160	310	16	
σ_z^{LD}	-1	1	2	Yes
ϕ_0	$\pi/16$	2π	32	
$\Delta E_Z^{\text{ST}}/h$ (MHz)	465	496	32	

Supplementary Table 2 | Parameter space for Equation 3.

The eight dimensional parameter space for evaluating Eq. 3. The search ranges of the five pulse-cycle-independent parameters are determined based on prior, coarse estimation results over wide spans.

Supplementary References:

- ¹Noiri, A., Yoneda, J., Nakajima, T., Otsuka, T., Delbecq, M. R., Takeda, K., Amaha, S., Allison, G., Ludwig, A., Wieck, A. D., and Tarucha, S. Coherent electron-spin-resonance manipulation of three individual spins in a triple quantum dot. *Appl. Phys. Lett.* **108**, 153101 (2016).
- ²Shafiei, M., Nowack, K. C., Reichl, C., Wegscheider, W., and Vandersypen, L. M. K. Resolving Spin-Orbit- and Hyperfine-Mediated Electric Dipole Spin Resonance in a Quantum Dot. *Phys. Rev. Lett.* **110**, 107601 (2013).
- ³Shulman, M. D., Harvey, S. P., Nichol, J. M., Bartlett, S. D., Doherty, A. C., Umansky, V., and Yacoby, A. Suppressing qubit dephasing using real-time Hamiltonian estimation. *Nat. Comm.* **5**, 5156 (2014).
- ⁴Nichol, J. M., Orona, L. A., Harvey, S. P., Fallahi, S., Gardner, G. C., Manfra, M. J., and Yacoby, A. High-fidelity entangling gate for double-quantum-dot spin qubits. *npj Quantum Information* **3**, 3 (2017).
- ⁵Petta, J. R. *et al.* Coherent Manipulation of Coupled Electron Spins in Semiconductor Quantum Dots. *Science* **309**, 2180-2184 (2005).
- ⁶Higginbotham, A. P., Kuemmeth, F., Hanson, M. P., Gossard, A. C., and Marcus, C. M., Coherent Operations and Screening in Multielectron Spin Qubits. *Phys. Rev. Lett.* **112**, 026801 (2014).
- ⁷Mehl, S. and DiVincenzo, D. P. Simple operation sequences to couple and interchange quantum information between spin qubits of different kinds. *Phys. Rev. B* **92**, 115448 (2015).
- ⁸Laird, E. A., Taylor, J. M., DiVincenzo, D. P., Marcus, C. M., Hanson, M. P., and Gossard, A. C. Coherent spin manipulation in an exchange-only qubit. *Phys. Rev. B* **82**, 075403 (2010).
- ⁹Nakajima, T., Delbecq, M. R., Otsuka, T., Amaha, S., Yoneda, J., Noiri, A., Takeda, K., Allison, G., Ludwig, A., Wieck, A. D., and Tarucha, S. Coherent transfer of electron spin correlations assisted by dephasing noise. *Nature Communications* **9**, 2133 (2018).
- ¹⁰Delbecq, R. M., Nakajima, T., Stano, P., Otsuka, T., Amaha, S., Yoneda, J., Takeda, K., Allison, G., Ludwig, A., Wieck, A. D., and Tarucha, S. Quantum Dephasing in a Gated GaAs Triple Quantum Dot due to Nonergodic Noise. *Phys. Rev. Lett.* **116**, 046802 (2016).
- ¹¹Dial, O. E., Shulman, M. D., Harvey, S. P., Bluhm, H., Umansky, V., and Yacoby, A. Charge Noise Spectroscopy Using Coherent Exchange Oscillations in a Singlet-Triplet Qubit. *Phys. Rev. Lett.* **110**, 146804 (2013).
- ¹²Meunier, T., Calado, V. E., and Vandersypen, L. M. K. Efficient controlled-phase gate for single-spin qubits in quantum dots. *Phys. Rev. B* **83**, 121403(R) (2011).
- ¹³Watson, T. F., Philips, S. G. J., Kawakami, E., Ward, D. R., Scarlino, P., Veldhorst, M., Savage, D. E., Lagally, M. G., Friesen, M., Coppersmith, S. N., Eriksson, M. A., and Vandersypen, L. M. K. A programmable two-qubit quantum processor in silicon. *Nature* **555**, 633–637 (2018).

¹⁴Shulman, M. D., Dial, O. E., Harvey, S. P., Bluhm, H., Umansky, V., Yacoby, A. Demonstration of Entanglement of Electrostatically Coupled Singlet-Triplet Qubits. *Science* **336**, 202-205 (2012).

¹⁵We used MATHEMATICA RADIA package available at <http://www.esrf.fr/> for MM field calculations.